Regulated structural transitions unleash the chaperone activity of αB-crystallin

Jirka Peschek[1], Nathalie Braun, Julia Rohrberg[2], Katrin Christiane Back, Thomas Kriehuber, Andreas Kastenmüller[3], Sevil Weinkauf, and Johannes Buchner[4]

Center for Integrated Protein Science and Department Chemie, Technische Universität München, 85748 Garching, Germany

Edited by Linda L. Randall, University of Missouri, Columbia, MO, and approved August 26, 2013 (received for review May 9, 2013)

The small heat shock protein αB-crystallin is an oligomeric molecular chaperone that binds aggregation-prone proteins. As a component of the proteostasis system, it is associated with cataract, neurodegenerative diseases, and myopathies. The structural determinants for the regulation of its chaperone function are still largely elusive. Combining different experimental approaches, we show that phosphorylation-induced destabilization of intersubunit interactions mediated by the N-terminal domain (NTD) results in the remodeling of the oligomer ensemble with an increase in smaller, activated species, predominantly 12-mers and 6-mers. Their 3D structures determined by cryo-electron microscopy and biochemical analyses reveal that the NTD in these species gains flexibility and solvent accessibility. These modulated properties are accompanied by an increase in chaperone activity in vivo and in vitro and a more efficient cooperation with the heat shock protein 70 system in client folding. Thus, the modulation of the structural flexibility of the NTD, as described here for phosphorylation, appears to regulate the chaperone activity of αB-crystallin rendering the NTD a conformational sensor for nonnative proteins.

sHsp | Hsp70 | conditional disorder | posttranslational modification | structure-function relationship

Molecular chaperones share the ability to bind nonnative, aggregation-prone polypeptides and assist their folding and assembly (1–3). Among these, the small heat shock protein (sHsp) αB-crystallin (also HspB5) is one of the major constituents of the vertebrate eye lens where it functions both as a chaperone and structural protein (4, 5). In nonlenticular tissues, αB-crystallin (αB) participates in sustaining cellular proteostasis. The involvement in neurodegenerative diseases (6, 7), multiple sclerosis (8), myopathies (9), as well as in cell cycle control, apoptosis, and cancer (10, 11) underlines its importance for cellular proteostasis.

αB exhibits a tripartite organization (Fig. 1*A*) with a central α-crystallin domain (ACD) flanked by an N-terminal domain (NTD) and a short C-terminal extension (CTE) (12, 13). The ACD forms stable dimers (14–16) that further assemble into higher-order oligomers via interactions mediated by the NTD and CTE (17–19). αB forms dynamic populations of multimers with a variable number of subunits (20, 21). Structural studies indicate that the variety of oligomeric states including a symmetric 24-mer (22) is created by addition of subunits to (or subtraction from) existing oligomers (17, 18). As for many other sHsps (23), the polydispersity of αB is coupled to spontaneous subunit exchange of yet undetermined units. αB quaternary dynamics was attributed to fluctuations of the intersubunit contacts mediated by the C-terminal IXI motif (24). However, given its involvement in oligomer formation, the NTD must also play a decisive role.

In general, sHsps including αB recognize aggregation-prone, partially unfolded substrates (4, 25, 26) and keep them in a refolding-competent state (27, 28). The substrate binding sites of sHsps have not been defined yet. Recent studies suggest the involvement of multiple sites from all three sequence regions (29–32). Due to the lack of structural information for the NTD, however, it is still not possible to propose a molecular mechanism for the mode of action of αB or sHsps in general. The emerging view is that their structural plasticity may be an important element in substrate recognition and binding (25, 29, 33–35). In this context, a key issue is to define how changes in the structural ensemble of αB correlate with chaperone function.

Because sHsps do not possess ATPase activity, their chaperone function is regulated by different means. For many mammalian sHsps, phosphorylation plays a major role in this context (36). For αB, the three major phosphorylation sites, Ser19, Ser45, and Ser59, all located within the NTD (Fig. 1*A*), are phosphorylated in response to various kinds of stresses (37, 38). Phosphorylation of αB has been shown to correlate with a reduction in average oligomer size and enhanced substrate binding (39–42). However, its influence on the molecular architecture and the underlying activation mechanism remained elusive.

To probe the role of the NTD of αB in oligomer assembly, equilibrium, and dynamics, as well as its impact on chaperone function, we used phosphomimicking mutants and phosphorylated αB. By destabilization of NTD interactions in larger oligomers, we were able to populate and identify the chaperone-active

Significance

The small heat shock protein αB-crystallin functions as an archetypical and ubiquitous molecular chaperone. It is an integral part of the cellular proteostasis system and associated with human diseases such as Alzheimer's disease, myopathy, cataract, and multiple sclerosis. The molecular architecture of αB-crystallin follows an intriguing construction plan characterized by a dynamic oligomer equilibrium. Here, we exploited phosphorylation mimetics as a tool to switch the protein to an activated functional state by a shift in the conformational ensemble. Using cryo-EM and image processing, we defined the structures of the activated αB-crystallin ensemble. Biochemical analysis revealed that, on activation, the N-terminal regions gain flexibility and solvent accessibility. This allows enhancing the activity of αB-crystallin and promoting its cooperation with the Hsp70 system.

Author contributions: J.P., S.W., and J.B. designed research; J.P., N.B., J.R., K.C.B., T.K., and A.K. performed research; J.P., N.B., J.R., K.C.B., and T.K. analyzed data; and J.P., S.W., and J.B. wrote the paper.

The authors declare no conflict of interest.

This article is a PNAS Direct Submission.

Data deposition: The cryo-EM density map of the αB-crystallin-3E (S19/45/59E) hexamer has been deposited in the Electron Microscopy Data Bank, www.ebi.ac.uk/pdbe/emdb (accession no. EMD-2366).

[1]Present address: Department of Biochemistry and Biophysics, University of California, San Francisco, CA 94158.

[2]Present address: Department of Cell and Tissue Biology, University of California, San Francisco, CA 94143.

[3]Present address: GATAN GmbH, 80807 München, Germany.

[4]To whom correspondence should be addressed. E-mail: johannes.buchner@tum.de.

This article contains supporting information online at www.pnas.org/lookup/suppl/doi:10.1073/pnas.1308898110/-/DCSupplemental.

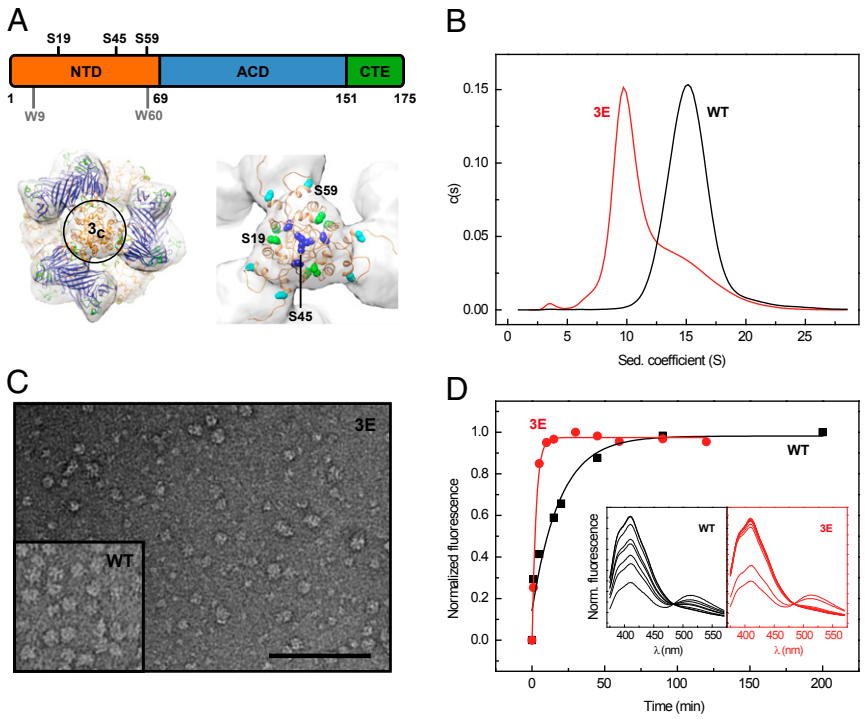

Fig. 1. Oligomer size, hydrophobicity, and quaternary dynamics of αB phosphomimics. (*A*) Domain organization of human αB: NTD (orange) with the three major in vivo phosphorylation sites Ser19, Ser45, and Ser59, ACD (blue), and CTE (green). (*Lower Left*) Surface representation of the cryo-EM density map of the αB 24-mer with the docked pseudoatomic model according to Braun et al. (17) superimposed (ribbon representation, domains colored as above). The molecule is viewed along a molecular threefold symmetry axis perpendicular to the area harboring the NTDs (closed threefold area, 3_c). (*Lower Right*) Close-up view of the pseudoatomic model at the area 3_c. The colored spheres depict residues S19 (green), S45 (blue), and S59 (cyan). (*B*) Analysis of αB-WT and its triple Glu mutant (αB-3E) by sedimentation velocity AUC. The *s*-value distributions of αB-WT (black) and αB-3E (red) obtained by c(s) analysis. (*C*) Transmission electron micrograph of αB-3E (0.02 mg/mL, pH 7.4) negatively stained with ammonium molybdate [1.5% (wt:vol), pH 5.5]. (Scale bar, 100 nm.) (*Inset*) TEM image of αB-WT (0.05 mg/mL) prepared as described for αB-3E. (*D*) Subunit exchange kinetics of αB-WT and αB-3E. Shown are the temporal changes in the donor fluorescence intensities at 415 nm due to reversal of FRET on adding excess amounts of unlabeled αB-WT (black) and αB-3E (red) to FRET-equilibrated heterooligomers of AIAS- and LYI-labeled αB-WT-S153C. αB-3E shows a higher subunit exchange rate (0.369 ± 0.028 min^{-1}) than αB-WT (0.053 ± 0.013 min^{-1}). The respective fluorescence spectra are depicted as insets in the same color code.

species in the remodeled ensemble and determine the structures of the active oligomers in which the structural flexibility and accessibility of the NTD emerged to be the key element for efficient binding as well as subsequent folding of clients.

Results

NTD of αB Plays a Decisive Role in Oligomer Integrity. Recent structural studies (17, 18) propose that αB oligomers are hierarchically assembled: the ACD mediates the formation of αB dimers, three of which constitute a hexameric unit stabilized through interactions using the C-terminal IXI motif (43). Such hexameric units associate further to higher-order multimers via N-terminal interactions. According to our pseudoatomic model of the αB 24-mer (17), the three major in vivo phosphorylation sites, Ser19, Ser45, and Ser59 of six NTDs, are all located in close proximity within one structural element (Fig. 1*A*) as confirmed here by disulfide cross-linking on replacement of the serines by cysteines (Fig. S1). This spatial proximity suggests a substantial destabilization of N-terminal intersubunit interactions on introduction of negative charges and hence significant implications on oligomer integrity. We exploited phosphorylation-mimicking mutants of αB in which these serines were replaced by glutamates to probe the role of the NTD in oligomer assembly and ensemble composition. All seven possible single (1E), double (2E), and triple (3E) glutamate (Glu) variants were recombinantly expressed in *Escherichia coli* and purified to homogeneity.

To examine the quaternary structures of the mutant proteins, we used size-exclusion chromatography (SEC), analytical ultracentrifugation (AUC), and electron microscopy (EM) (for details, see *Materials and Methods*). SEC indicated a reduction in the mean oligomer size of the Glu variants compared with WT αB (αB-WT; Fig. S2*A*). Consistently, sedimentation velocity (SV) AUC experiments revealed a shift of the weight average sedimentation coefficient ($<s_{20,w}>$) from 16.1 S for αB-WT (Fig. 1*B*) toward smaller values for all Glu variants (Fig. S2*B*; Table S1). The triple mutant αB-3E displayed an asymmetric distribution indicative for the presence of at least two populations of different oligomeric species (Fig. 1*B*). An additional small peak at 3 S for αB-3E suggested the presence of dimeric species. Radial concentration distributions derived from sedimentation equilibrium (SE) AUC experiments confirmed that αB-WT and αB-3E differ in their average molecular masses (490 vs. 330 kDa) under equilibrium conditions (Fig. S2*C*). To investigate the changes in oligomer sizes in more detail, we subjected αB-WT and its phosphorylation-mimicking variants to negative stain EM (NS-EM) and determined their size distributions (Fig. S2*D*). All Glu variants showed a shift toward smaller oligomers. αB-3E contained a large fraction of smaller oligomers compared with αB-WT (Fig. 1*C*).

To test how destabilization of N-terminal subunit contacts affects the quaternary dynamics of αB, we performed FRET studies. To this end, donor- and acceptor-labeled αB-WT-S153C oligomers were mixed and incubated until a FRET equilibrium was reached. On adding excess amounts of unlabeled αB-WT or αB-3E to these FRET heterooligomers, an increase in donor fluorescence was observed with time due to subunit exchange (SX) (Fig. 1*D*). Using an exponential model for SX kinetics (23),

rate constants of 0.053 ± 0.013 and 0.369 ± 0.028 min^{-1} were obtained for αB-WT and αB-3E, respectively, indicating enhanced quaternary dynamics in the phosphorylation-mimicking mutant in agreement with previous suggestions (40). Similar to the average oligomer size, SX rates also suggest a correlation with the number of introduced Glu residues (Fig. S2*E*; Table S1).

To provide further evidence for heterooligomer formation between αB-WT and αB-3E, we performed fluorescence AUC using Atto488-labeled αB-WT and unlabeled αB-3E. When increasing amounts of unlabeled αB-3E were added to labeled αB-WT, the size distribution shifted gradually toward the one of αB-3E (Fig. S2*F*). As the use of fluorescence optics allowed selective monitoring of the labeled αB-WT subunits, this shift can only be explained by the formation of mixed complexes.

Impairment of N-Terminal Interactions in αB Oligomers Leads to Dissociation of Hexameric Units from Higher-Order Oligomers. The reduction in the average oligomer size of phosphorylation-mimicking mutants does not necessarily imply that the small oligomers observed for the Glu variants are due to the partial dissociation of the higher-order multimers as present in αB. They may also form on charge-induced structural rearrangements and obey assembly principles different from the WT protein. Resolving the structures of the smaller oligomers is thus of central importance for delineating the chaperone mechanism of αB-crystallin. To this end, we performed cryo-EM and image processing of the 3E variant. The projection images of αB-3E oligomers in cryo electron micrographs (Fig. S3*A*) resembled those previously determined for αB-WT (17). A model-free separation of the αB-3E data by multivariate statistics [multivariate statistical analysis (MSA)] and classification indicated the presence of various αB-3E assemblies with sizes and structural features similar to αB-WT oligomers (Fig. S3 *C–F*). This observation justified further sorting of the data using previously calculated oligomer models of αB-WT as initial references. This way, we could unambiguously assign ∼80% of the particle images to distinct αB-3E oligomers and calculate 3D models of the most populated oligomers, i.e., 6-, 12-, and 24-mers, by projection matching cycles (Fig. 2*A*; Table S2). It should be noted that methodological limitations prevented the analysis of species smaller than hexamers, such as dimers.

According to our reconstructions, the oligomer structures observed for αB-3E (Fig. 2*A*) and αB-WT (Fig. 2*B*) are consistent. The αB-3E 24-mer is, like its αB-WT counterpart, a hollow, spherical complex with tetrahedral (P23) symmetry characterized by openings at positions of the twofold symmetry axes and at one of the two areas where a threefold symmetry axis intercepts the protein shell (open threefold area, 3_o; Fig. 2*A*). In addition, the mass-rich area at the position of the opposite intercept of the threefold axis (closed threefold area, 3_c) and the characteristic relief surrounding 3_o are also well preserved in the αB-3E 24-mer. The structures of 12- and 6-mers of both αB-WT and αB-3E also show a striking resemblance. The 6-mers are characterized by a symmetric (C3), ring-like arrangement of three structural units each possessing an "arm" pointing downward from the ring, whereas the 12-mers are composed of two adjacent 6-mers interconnected by two bridging densities (Fig. 2). From the parity of the corresponding oligomer structures of αB-WT and αB-3E, it is obvious that the hierarchical "dimer-hexamer-multimer" architecture and the subunit organization of αB oligomers are conserved in the 3E mutant. However, the relative oligomer populations of αB-3E differ substantially from those observed for αB-WT (Fig. S3*H*): whereas the symmetric 24-mer contributes to ∼42% of the αB ensemble, it constitutes only ∼6% of αB-3E particles. On the other hand, the species present at low abundance in the WT protein, mostly 6- and 12-mers, contribute together up to ∼65% of αB-3E particles. The predominance of the species composed of hexameric building blocks along with the conserved subunit organization in αB-3E oligomers clearly indicates an enhanced tendency for dissociation of the higher-order αB-3E oligomers at the hexamer assembly sites accommodating the NTDs.

According to our model, additional negative charges in the NTD should further weaken the interactions that contribute to the assembly of larger oligomers. To test this, we constructed an αB variant harboring six phosphomimetic Ser-to-Glu mutations (αB-6E) at positions 19, 21, 43, 45, 53, and 59 (44). In this variant, the formation of higher-order oligomers such as 24-mers was almost completely suppressed. The weight-average sedimentation coefficient of 6.3 S for αB-6E as determined by AUC (Fig. S4*A*; Table S1) along with the sedimentation coefficient of 6.0 S for hexameric species as predicted by hydrodynamic

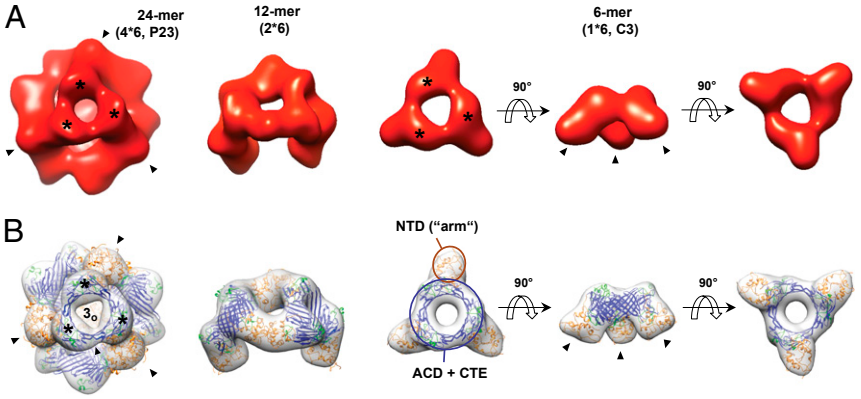

Fig. 2. Hierarchical assembly principle of αB oligomers is preserved in the phosphomimic αB-3E. (*A*) 3D reconstructions of αB-3E oligomers observed in cryo-EM. The isosurface threshold was set to enclose a molecular mass of 485 kDa for the 24-mer, 242 kDa for the 12-mer, and 121 kDa for the 6-mer. (*B*) 3D reconstructions of αB 24-, 12-, and 6-mer with the docked pseudoatomic models according to Braun et al. (17) superimposed (ribbon representation, domains colored as in Fig. 1*A*). Note that only the 24-mer pseudoatomic model is energy-minimized. 24-mers are viewed along a threefold symmetry axis intercepting the area harboring a window (open threefold area, 3_o). Mass-rich domes surrounding 3_o and accommodating the CTEs are highlighted by stars and threefold symmetric areas where the NTDs are located (closed threefold area, 3_c) by closed arrows. 12-mers are viewed almost perpendicular to an axis that corresponds to the twofold symmetry axis of the 24-mer. The 6-mers are shown in three different orientations (top, side, and bottom views). All reconstructions are presented at a resolution of 18 Å to improve comparability. Note the consistency of the oligomer structures of αB-3E and αB-WT.

simulations (Table S2) indicated that αB-6E ensemble consisted of mainly hexamers.

Taken together, these results underline the importance of the NTD in modulating the oligomer equilibrium and dynamics of αB as the destabilization of NTD-mediated subunit interactions leads to enhanced SX dynamics and results in a remodeling of the ensemble composition.

NTD of αB Exhibits Conditional Disorder. As a consequence of the dissociation of higher-order αB-3E oligomers into smaller species, a considerable amount of NTDs is no longer engaged in oligomer interactions and thus may undergo structural alterations and/or possess changed accessibilities. To assess the latter in the context of the αB-3E ensemble, we monitored fluorescence quenching by acrylamide of the intrinsic probes Trp9 and Trp60, which are the only tryptophan residues in the αB sequence and are both located within the NTD (Fig. 1*A*). Titration experiments revealed a larger quenching effect for αB-3E compared with αB-WT, pointing to an increased solvent accessibility of both tryptophan residues (Fig. 3*A*).

To assess the dissociation-induced changes in overall surface hydrophobicity, we monitored the fluorescence of the environment-sensitive dye 8-anilino-1-naphthalene sulfonate (ANS) on binding to αB. The ANS fluorescence emission intensity was increased in the presence of αB-3E compared with αB-WT (Fig. 3*B*). As ANS binding to proteins involves mainly hydrophobic interactions (45), the spectra indicate either an increased exposure of hydrophobic regions, most of them located in the NTD (Fig. 3*B*, *Inset*), or a gain in structural flexibility allowing local rearrangements to accommodate the dye (46). A combination thereof appears conceivable as well.

To further probe conformational features of the NTD in the context of the αB-3E ensemble, we used limited proteolysis experiments. For this, αB-WT and αB-3E were incubated with α-chymotrypsin, and the proteolytic digestion was analyzed at various time points by SDS/PAGE (Fig. 3*C*). The experiments indicated a faster degradation rate for the phosphomimetic

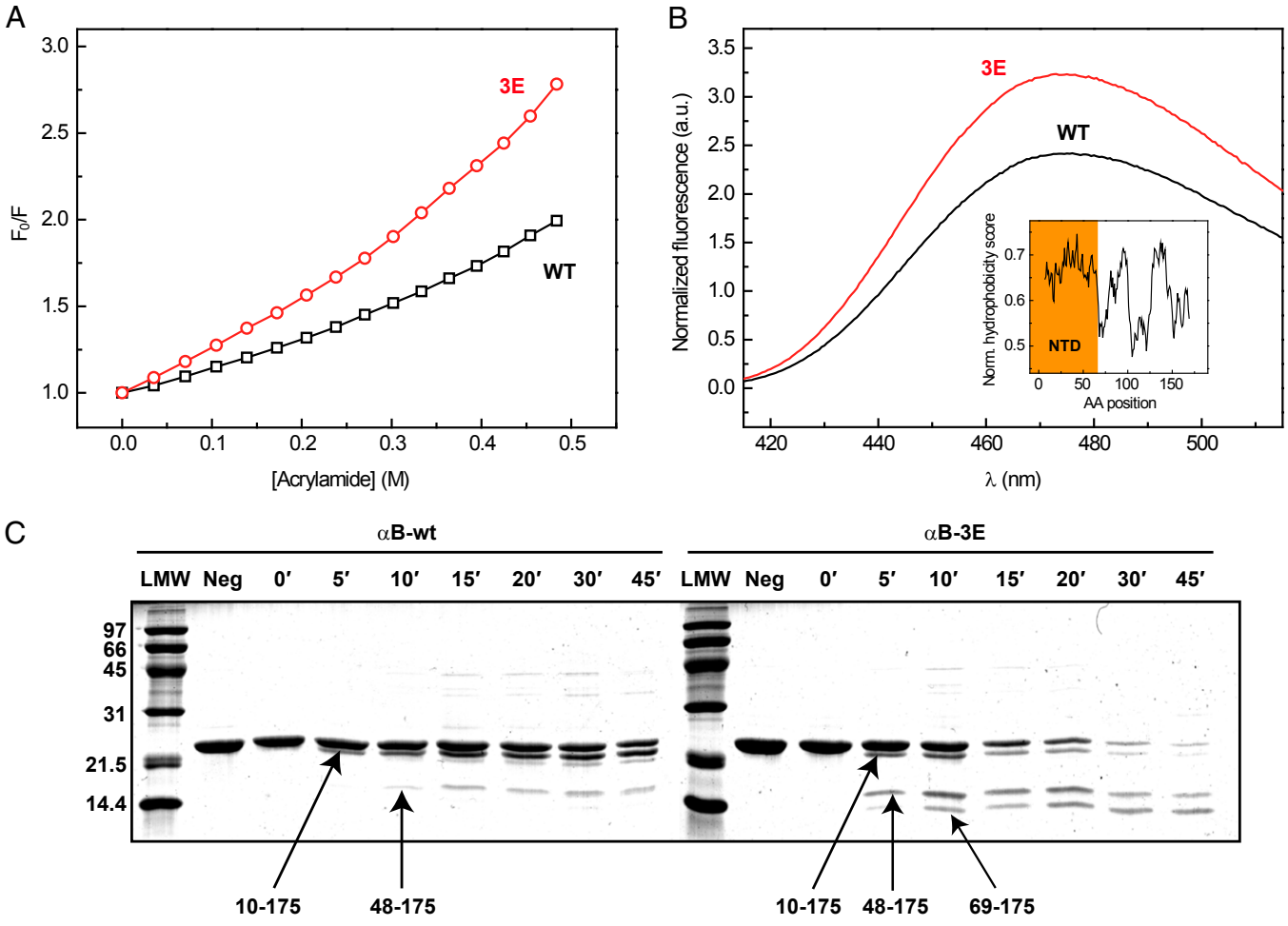

Fig. 3. Conformational properties of the NTD in αB-3E. (*A*) Quenching of intrinsic tryptophan fluorescence by acrylamide. Fluorescence of the intrinsic Trp probes (Trp9, Trp60) of αB-WT (black squares) and αB-3E (red circles) was quenched by acrylamide. The Stern-Volmer plot (relative decrease in fluorescence [F_0/F] vs. quencher concentration) shows more quenching for the tryptophan residues in the context of αB-3E ensemble indicating higher accessibility. (*B*) Overall surface hydrophobicity of αB-WT (black) and αB-3E (red) probed by ANS fluorescence. Note the increased fluorescence intensity of αB-3E compared with αB-WT indicating a gain in overall surface hydrophobicity. (*Inset*) Hydrophobicity plot of αB sequence. The sequence segment representing the NTD is colored orange. The hydrophobicity score was calculated on the basis of a hydrophobicity scale by Eisenberg et al. (70) using the web-based application ProtScale (71). (*C*) Limited proteolysis of αB-WT (*Left*) and αB-3E (*Right*) by α-chymotrypsin. Protein samples (10 μM) were incubated with α-chymotrypsin at a 1:25 (wt/wt) ratio. Proteolysis reactions were terminated after various time points and analyzed by SDS/PAGE. The cleavage products were identified using LC-MS. The respective bands are indicated by an arrow and labeled with the identified peptide. Samples without chymotrypsin (Neg) were included as control. LMW, low-molecular-weight marker.

mutant compared with αB-WT. αB-3E was almost completely degraded after 45 min, whereas the band of full-length αB-WT was still present (Fig. 3*C*). Importantly, the proteins also differed in their cleavage patterns. MS analysis of the major peptide products of the proteolytic cleavage revealed W9, F47, and M68 as the three major proteolysis sites for αB-3E and only the former two for αB-WT (Fig. S5). The band corresponding to fragment 10–175 was formed with similar kinetics for both proteins (Fig. 3*C*). However, fragment 48–175 appeared more rapidly for the phosphomimicking mutant compared with αB-WT (Fig. 3*C*). The difference was even more pronounced for fragment 69–175, which was present in αB-3E already after a 10-min incubation but could not be detected for αB-WT in the course of the experiment (Fig. 3*C*). These results strongly suggest that the NTD adopts different conformational states in αB-WT and αB-3E: whereas the most N-terminal αB chain segment harboring the cleavage site W9 apparently possesses similar accessibilities, the segments including the sites F47 and M68 seem to gain in (backbone) flexibility in αB-3E and thus become exposed for proteolytic attack.

The indications for an enhanced flexibility of the NTD in αB-3E prompted us to analyze the structures of 6- and 12-mers in more detail. For this purpose, we first subjected the αB-3E 6-mer data set to a 3D-MSA, a method that accounts for variances and allows elucidating dynamics (47). The analysis revealed various 3D class averages that obviously represent different conformational states of αB-3E 6-mers (Fig. 4*A*). All structures have in common the characteristic ring-like structure formed by three ACD dimers (Fig. 4*A*, first row). However, they differ strikingly at terminal regions of the arms that harbor the NTDs from neighboring ACD dimers (Fig. 4*A*, second row). In some populations, these segments are disconnected and point toward the exterior or interior of the structure, whereas in others, they contact each other to partly close the opening of the central ring on one side (Fig. 4*A*, second row). The analysis of the 12-mer population also revealed pronounced structural variances. In addition to substantial movements of the terminal arm regions as observed in the 6-mer reconstructions, the relative orientations of the two hexameric units of the 12-mer show major variances indicating significant flexibilities also in the hinge regions harboring the NTDs and connecting the 6-mers (Fig. 4*B*).

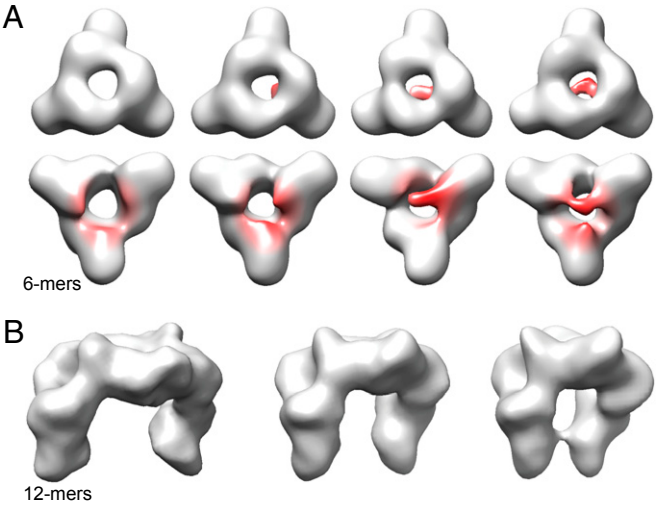

Fig. 4. Structural variance of small αB-3E oligomers. (*A*) Surface representations of the cryo-EM density maps (C1 symmetry) of αB-3E 6-mers in different conformational states. The isosurface thresholds were set to enclose a molecular mass of 121 kDa. Model orientations correspond to the orientation of the hexameric unit in αB-WT 24-mer when viewed from outside (first row; top view) (Fig. 2) or from inside (second row; bottom view). The areas of highest variances are colored red. Note the consistency of the ring-like structure (first row) built of three ACD dimers and the flexibility at terminal regions of the arms harboring NTDs (second row). (*B*) Surface representations of the cryo-EM density maps of αB-3E 12-mers in different conformational states. Note the (slight) variances in relative orientations of the two hexameric units indicating flexibility in hinge regions and the substantial variances in the relative positions of N-terminal arms ranging up to a partial closure of the otherwise open 12-mer structure.

The presence of multiple 6- and 12-mer structures with conformationally variable NTDs indicate flexibility in the NTDs when exposed and more rigidity in the higher-order oligomers.

NTD of αB Is Crucial for Substrate Binding and Chaperone Activity. Phosphorylation has been described to affect the chaperone activity of αB (40, 41, 48). The predominance of smaller species with flexible NTDs on phosphomimicking, as shown here, implies an important role of N-terminal conformation in chaperone activity. A crucial question is whether the smaller species are indeed the chaperone-active forms. To test this, we analyzed the chaperone activity of αB-3E using malate dehydrogenase (MDH) as a model substrate and the tumor suppressor p53 as a physiological client. The latter is known to be aggregation-prone at elevated temperatures in vitro (49, 50) and to be associated with αB in vivo (51). The chaperone assays showed that αB-3E is more potent in suppressing the temperature-induced aggregation of MDH and maintaining it in the soluble fraction than equivalent concentrations of αB-WT (Fig. S6 *A* and *B*). Consistent with this result, the suppression of heat-induced aggregation of p53 also showed a strong dependency on the phosphomimicking substitutions. Although αB-WT was incapable of preventing the thermal aggregation of p53, αB-3E efficiently suppressed the formation of light-scattering, insoluble aggregates already at substoichiometric concentrations (Fig. 5 *A* and *B*). αB-1E and αB-2E variants exhibited intermediate activities depending on the number of introduced Glu residues (Fig. S6*C*). To substantiate the in vivo relevance of these findings, we enzymatically phosphorylated αB in vitro using purified mitogen-activated protein kinase-activated protein (MAPKAP) kinase 2. Hsp27 and αB were shown to be substrates of this kinase in vivo (38, 52). Two Ser residues within αB, Ser-53 and Ser-59, are present in the preferred peptide sequence of MAPKAP kinase 2, Hyd-X-Arg-X(2)-Ser (where Hyd is a large hydrophobic residue). We confirmed the modification using Phos-tag gels (Fig. S4*B*). Phosphorylated αB (αB-phospho) exhibited a decrease in average oligomer size (Fig. S4*A*) and an increased chaperone function evidenced by the more effective aggregation suppression toward MDH (Fig. S6*A*) and p53 (Fig. S6*C*).

Using FRET SX kinetics (Fig. 1*D*) and fluorescence AUC experiments (Fig. S2*F*), we showed that αB-WT and αB-3E dynamically exchange subunits to form mixed oligomers. Interestingly, the chaperone activity toward p53 was reduced for WT/3E heterocomplexes with increasing amounts of αB-WT while keeping the total concentration of αB-3E constant (Fig. S6*D*). Thus, the holdase activity of αB is not determined by the total amount of phosphomimicking subunits but rather by the properties of the oligomers, more precisely the average conformational state of the NTDs.

To identify the binding-competent species within the αB-3E ensemble, we labeled p53 with a fluorescent dye (FAM), allowed p53-αB-3E complexes to form, and analyzed them by SV-AUC. Using a fluorescence detection system, we specifically monitored free p53-FAM and all complexes containing p53-FAM. According to the c(s) distributions (Fig. 5*C*), the calculated s-value of p53-FAM shifts from 4.9 S to 11 S in the presence of αB-3E. Moreover, αB-3E/p53-FAM complexes range in size between αB-3E and αB-WT, with the maximum of the distribution being 1 S larger than αB-3E. The results imply a preferential binding of p53 to smaller αB-3E oligomers and support the notion of

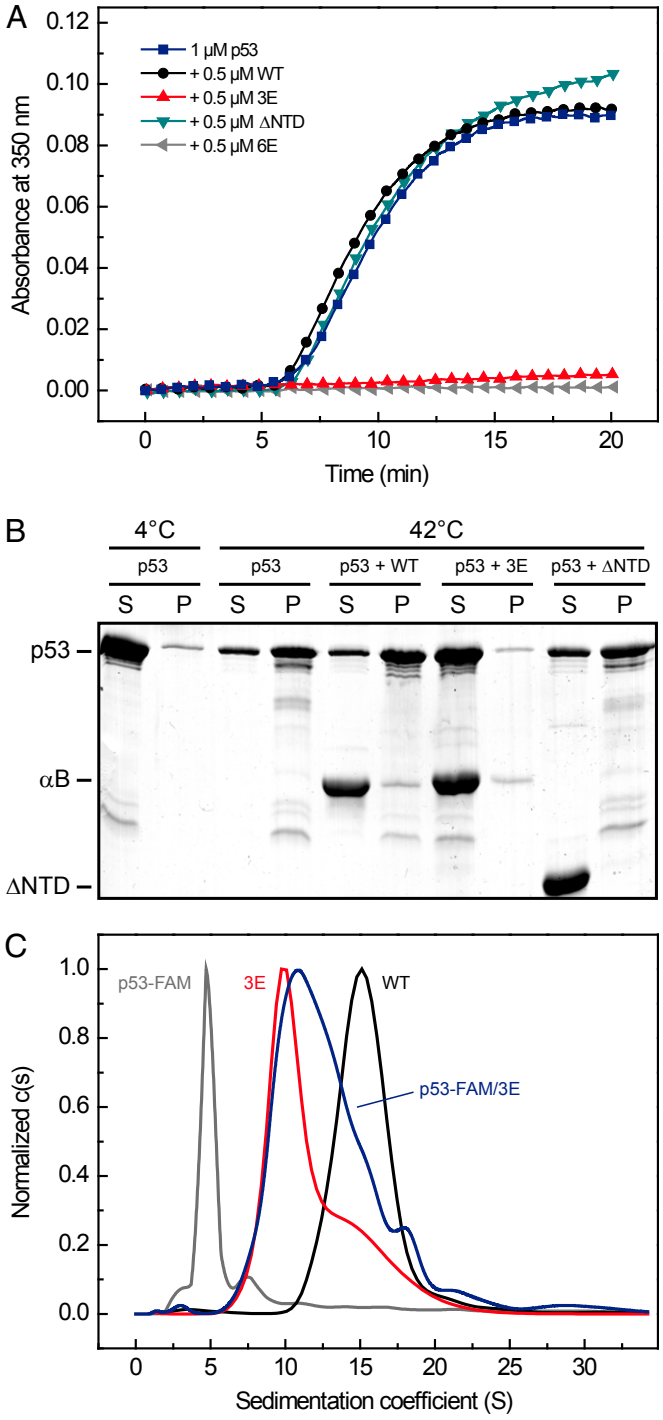

Fig. 5. Effects of mimicking phosphorylation on the chaperone function. (*A*) Aggregation of p53. The aggregation of 1 μM p53 (blue) was induced by heat shock at 42 °C and monitored by absorbance at 350 nm. The chaperone activity of αB-WT (black), αB-3E (red circles), the N-terminal deletion mutant αB-ΔNTD (teal), and αB-6E (gray) was assessed in the presence of 0.5 μM of the respective αB variant. Note the inability of αB-WT and αB-ΔNTD in suppressing the formation of light-scattering aggregates. (*B*) SDS/PAGE of the soluble [supernatant (S)] and insoluble [pellet (P)] fractions of p53 aggregation assays after separation by centrifugation (10 min, 10,000 × *g*). Although a large fraction of p53 is found in the pellet fraction in the presence of αB-WT, αB-3E is able to keep almost all p53 in soluble substrate/chaperone complexes. Note that αB-ΔNTD is unable to bind p53. (*C*) Fluorescence SV-AUC analysis of FAM-labeled p53 alone (gray) and in complex with αB-3E (blue). According to the c(s) distributions, the complexes range in size between αB-3E (red) and αB-WT (black).

a crucial role of N-terminal flexibility in recognition and binding of p53. The functional importance of the NTD for the chaperone function of αB is further substantiated by the observation that a mutant, in which the NTD was deleted (αB-ΔNTD), was incapable of suppressing the heat-induced aggregation of p53 (Fig. 5*A*) and MDH (Fig. S6*A*). Although αB-ΔNTD assembles, similar to αB-6E, into small oligomeric species (Fig. S4*A*), it did not form stable substrate complexes or coaggregate with the clients (Fig. 5*B*; Fig. S6*B*). Despite the large number of introduced negatively charged Glu residues, αB-6E exhibited the most efficient aggregation suppression toward both tested substrates (Fig. 5*A*; Fig. S6*A*). Thus, the structural flexibility and solvent accessibility of the NTD in the context of small oligomers is essential for client binding and not the existence of small oligomers per se.

To test whether the enhanced ability of αB-3E to recognize and bind heat-destabilized substrate proteins is not limited to clients in vitro but is a general characteristic, we subjected HeLa cell lysates to heat stress and analyzed the soluble and insoluble fractions by SDS/PAGE. In the absence of αB-WT or αB-3E, a large portion of lysate proteins was found in the insoluble fraction (Fig. S6*E*). In the presence of αB variants, a larger portion of the protein was found in the soluble fraction. Lower concentrations of αB-3E were required to generate this effect compared with αB-WT (Fig. S6*E*). The analysis of the pellet fraction by electrospray ionization MS (ESI-MS) yielded more than 300 proteins belonging to the heat-sensitive fraction of the proteome protected by αB (see Dataset S1 for full list), indicating a rather promiscuous binding to unfolding polypeptides in agreement with a general function of αB in proteome protection.

N-Terminal Flexibility Facilitates Client Reactivation by the Hsp70 System. For efficient refolding of sHsp-stabilized nonnative proteins, the cooperation with ATP-dependent chaperones is required (27, 28, 53). To elucidate whether the modulated properties of the NTD in αB-3E affect client refolding by the Hsp70 system, we monitored the regain of enzyme activity for MDH in the presence of Hsc70 and Hdj1 as the refolding system and either αB-WT or αB-3E as the holdase. As expected, client release and refolding were strictly dependent on the presence of ATP and both Hsc70 and Hdj1 were required (Fig. 6). Interestingly, an almost twofold higher final yield of MDH was observed in the presence of αB-3E compared with αB-WT, although in each case, MDH aggregation had been suppressed completely (Fig. 6, *Inset*).

In the case of p53, an EMSA was used to probe the refolding of heat-denatured p53 via its DNA binding ability. Here also, ATP-dependent refolding of p53 by Hsc70 and Hdj1 was observed when the thermal inactivation was performed in the presence of αB-3E (Fig. S7), whereas αB-WT did not allow for p53 reactivation. Similar to the results with MDH, neither Hsc70 nor Hdj1 alone was sufficient for reconstituting DNA binding-competent p53.

From the results above, we conclude that the enhanced N-terminal flexibility in the αB-3E ensemble is not only crucial for the promiscuous binding to unfolding polypeptides but also facilitates their reactivation by the downstream ATP-dependent chaperones.

Discussion

sHsps constitute an ancient and efficient protective system capable of binding unfolding proteins under conditions of proteotoxic stress (54–56). The majority of sHsps, among them also human αB, show an unusual structural plasticity (21). To understand the contribution of sHsps to the chaperone machinery of the cell, it is a prerequisite to uncover the mechanistic link between their structure, dynamics, and the regulation of substrate binding and chaperone activity.

As phosphorylation is often coupled to conformational changes and all major in vivo phosphorylation sites of αB are located within

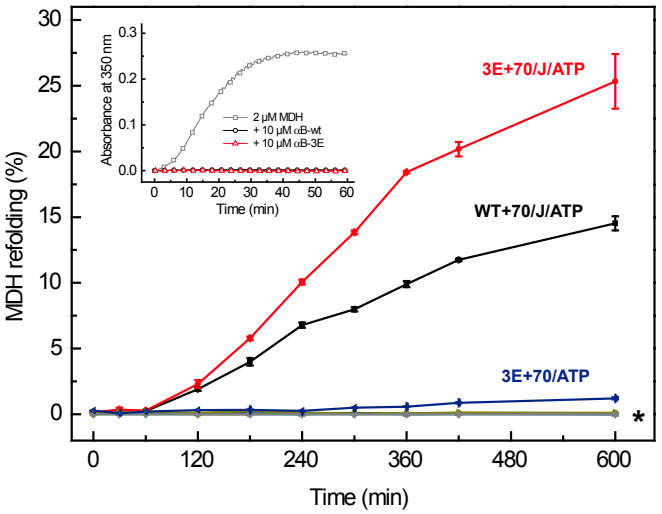

Fig. 6. Substrate binding and interplay with the Hsp70 chaperone system in client remodeling. MDH was denatured at 46 °C in the absence and in the presence of αB-WT and αB-3E. The inactive MDH was subsequently reactivated in the presence of a mixture of human Hsc70 (70) and the Hsp40 cochaperone Hdj1 (J) and an ATP-regenerating system. Reactivation of MDH was assessed by its enzymatic activity. Refolding yields are based on the activity of a native control that was equally treated. The samples without any refolding component, with Hdj1/ATP, and with Hsc70/Hdj1/no ATP, which did not yield any refolding, are marked with an asterisk. (*Inset*) Experimental conditions ensured complete aggregation suppression of MDH.

its NTD, we reasoned that the NTD provides key switch points for conformational changes. We used different experimental approaches to characterize various αB phosphomimicking mutants. As discussed below, these results revealed a dual role for the NTD in the mechanism of αB: it contributes decisively to the assembly and dynamics of αB oligomers and acts as a tunable conformational sensor in regulating αB activity (Fig. 7).

The reduction in the average oligomer size of phosphomimicking mutants compared with that of αB, together with cysteine cross-linking and FRET assays, suggests that the close proximity of the introduced negative charges in the NTD destabilizes oligomer contacts, which, in turn, leads to enhanced SX rates through accelerated dissociation of higher-order oligomers. Previously, fluctuations in binding of the C-terminal IXI motif to a hydrophobic groove within the ACD of a neighboring monomer have been reported to determine the subunit exchange process in αB (24). Although a contribution of this interaction to the oligomer dynamics is likely, our results and those obtained for other sHsps (33, 57) suggest an important role of the intersubunit contacts mediated by the NTDs in oligomer dynamics.

Our structural studies using cryo-EM/single particle analysis reveal that the modular assembly principle of αB (17, 18) remains conserved in the mutant αB-3E. A notable characteristic of the αB-3E ensemble is the predominance of species composed of hexameric building blocks, e.g., 6- and 12-mers, due to the enhanced tendency for dissociation of the higher-order oligomers at the hexamer assembly sites accommodating the NTDs. From the 3D reconstructions of 6- and 12-mers, it is obvious that introduction of charges into the NTD does not largely affect subunit interactions mediated by ACDs, which lead to the formation of αB dimers, nor interactions mediated by CTEs as their organization into hexameric units remains intact.

An intriguing finding from our studies is the increased flexibility of NTDs in smaller αB-3E oligomers and the increase in the overall surface hydrophobicity. In the phosphomimetic variant, the dissociation of higher-order oligomers renders NTDs solvent-accessible and allows them to sample multiple conformational states. This situation is best described as an order-to-disorder transition of the NTDs: They are more confined when engaged in intersubunit interactions in higher-order oligomers and more disordered when exposed to the solvent in smaller species. Order-to-disorder transitions have also been found in the context of client interactions for other chaperones (58–60). In general, intrinsically disordered regions are known to promote binding promiscuity and may thus be important for the ability of chaperones to bind clients differing in structure and sequence (61–63). For αB, the structural flexibility of the NTD would therefore explain the observed promiscuity in adapting to multiple clients. Because phosphorylation sites within the flexible NTD were detected for many mammalian sHsps, it is tempting to speculate that the described activation mechanism is of general relevance. In addition, posttranslational modifications in eukaryotic proteins occur preferentially in disordered regions (61), with ~75% of the phosphorylation sites being found outside known Pfam domains (64).

The functional consequence of the increase in smaller oligomers with flexible NTDs in αB-3E is a more efficient chaperone activity. For the interaction with nonnative proteins, the exposure of hydrophobic residues in the NTD is presumably important because the mutant lacking the entire NTD is incapable of forming stable substrate complexes. It is most likely that the NTDs display similar properties in αB-WT. However, as the oligomers with "free" NTDs occur only at low abundance in the αB-WT ensemble, their contribution to the chaperone activity will be rather low. This conclusion is consistent with the reduced binding affinity of αB under normal conditions and supports the view that the overall properties of αB are dictated by the relative frequencies of activated and dormant storage assemblies. The conformational state of the NTD is also important for downstream processes in the cell (65). Our results reveal that the folding of αB-bound clients by Hsp70 and Hsp40 is more efficient for smaller αB oligomers. The chaperone system used in our study cannot completely mimic the sophisticated cellular folding machinery. For example, Hsp90 presumably plays a role in p53 folding in vivo (66, 67). We show that the Hsp70/40 system cooperates more efficiently with the 3E mutant compared with WT αB-crystallin. The more productive refolding suggests that αB-3E either binds substrates in a different conformation or facilitates the accessibility for the Hsp70 system.

The negative charges introduced by phosphorylation (mimetics) in the NTD do not seem to negatively influence client interactions. With regard to the impact on structure and function, we could not observe major differences between the studied phosphorylation sites. In vivo, most of the phosphorylated forms of αB were found to be modified at one or two serine residues (37). The different Glu mutants exhibit activities that correlate with the amount of introduced phosphomimicking residues. Hence, the existence of multiple sites, which undergo differential phosphorylation in response to diverse stress conditions, might allow tuning of the binding affinity of αB toward unfolded proteins according to the demands of the cell.

In summary, the view supported by our results suggests that the structural flexibility of the NTD enables αB to function as a tunable conformational sensor toward nonnative proteins. It remains to be determined whether other triggers also activate the chaperone function of αB or sHsps according to this principle.

Materials and Methods

Cloning and Protein Purification. All variants of αB were cloned and purified as established previously (22). αB-ΔNTD (residues 67–175) was purified using a similar protocol as for αB-WT using a Superdex 75-pg column (GE) as a second purification step. Hsc70 was purified as described elsewhere (68) using a Superdex200 SEC column (GE) as an additional last step. For *Hdj1* gene expression, *E. coli* BL21(DE3) was transformed with a Hdj1-pET21b plasmid, and the cells were grown at 37 °C and induced by 1 mM isopropyl β-D-1-thiogalactopyranoside (IPTG). Cleared lysate was applied on an SP

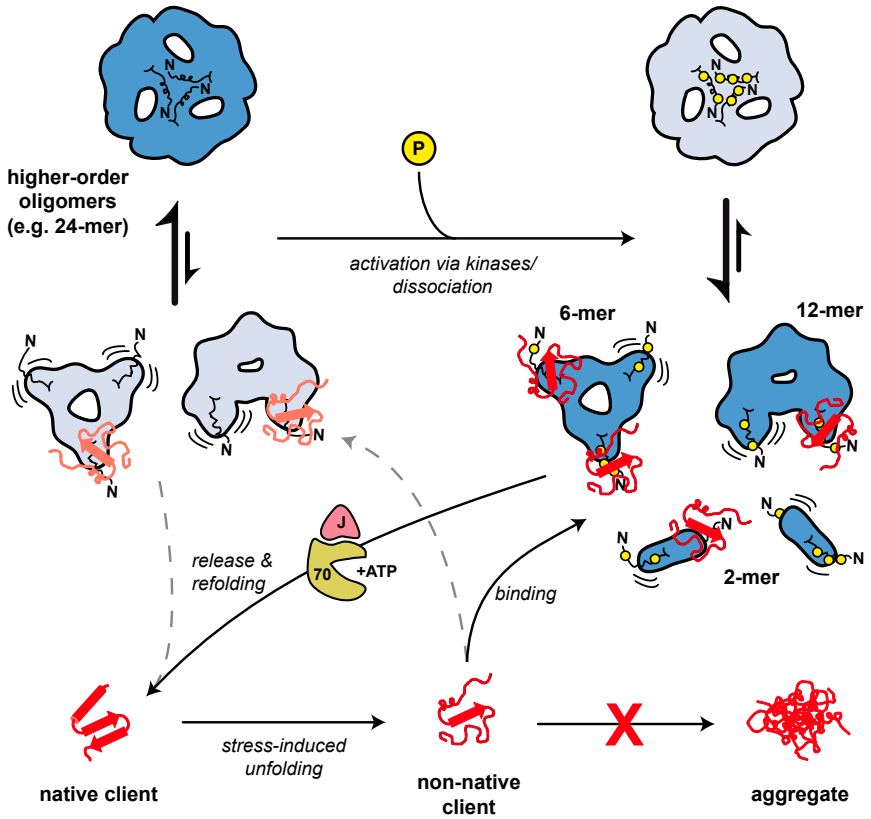

Fig. 7. A model for the chaperone mechanism of αB. The unmodified WT protein forms mainly higher-order oligomers like the symmetric 24-mer shown here. The predominant αB species in the oligomer equilibrium are depicted in dark blue; less abundant ones are in light blue. In response to stress, kinases activate αB by phosphorylation within the NTD (indicated by yellow circles), which leads to the partial dissociation into smaller oligomers, predominantly 12-mers, 6-mers, and dimers. In these species, the NTDs, which are characterized by an increased flexibility and accessibility, mediate efficient binding of nonnative clients. The formation of stable αB-client complexes prevents protein aggregation and creates a reservoir of folding-competent client molecules for the ATP-dependent refolding by the Hsp70 chaperone machine. However, due to the presence of a minor population of smaller oligomers with accessible NTDs, αB-WT also exhibits a basal chaperone activity toward nonnative proteins. Whether higher oligomers also are active chaperones remains to be determined.

Sepharose column (GE) equilibrated with TE buffer (50 mM Tris and 2 mM EDTA, pH 7.5). The pooled fractions were loaded onto a Superdex 200-pg column run in PBS. Human p53 was cloned and purified as described previously (69).

Quaternary Structure Analysis. The quaternary structure analysis of all αB variants was carried out by analytical gel filtration (SEC) and AUC as described previously (17, 22). For a detailed description, see *SI Materials and Methods*.

EM and Image Processing. Negative staining experiments were conducted as described previously (17, 22). For cryo-EM, 3 μL of protein solution (0.2 mg/mL) was applied onto glow-discharged holey carbon grids (Quantifoil, Multi A) and plunge-frozen in liquid ethane on blotting away the excess solution. Micrographs were recorded under low-dose conditions and at a calibrated magnification of 49,500× using a JEOL JEM- 2011 transmission electron microscope operated at 120 kV.

3D reconstructions of 6-, 12-, and 24-mers were performed by projection matching cycles as described previously (17). For further details on image processing, see *SI Materials and Methods*.

Extrinsic and Intrinsic Fluorescence. For the ANS binding studies, 10 μM protein was mixed with 1 mM ANS in PBS buffer. Fluorescence spectra were recorded using a FluoroMax 3 spectrometer (Jobin-Yvon) at 37 °C in the wavelength range from 400 to 520 nm on excitation at 372 nm. The signal intensity after addition of ANS was constant over more than 2 h, and the presence of ANS did not affect the oligomer equilibrium as validated by SV-AUC.

Fluorescence of the intrinsic probe Trp60 was quenched by stepwise addition of acrylamide (5 M) in the presence of 20 μM protein. The fluorescence was monitored with a Fluoromax 3 (Jobin Yvon). The experiments were carried out at 37 °C in PBS buffer.

Subunit Exchange Kinetics. The S153C mutant of αB-WT was labeled with lucifer yellow iodoacetamide (LYI) and 4-acetamido-4′-[(iodoacetyl)amino] stilbene-2,2′disulfonic acid (AIAS) (both from Molecular Probes) according to the manufacturer's protocol for 2 h at room temperature in PBS. Unbound label molecules were removed using a HiPrep 26/10 Desalting Column (GE). The donor- and acceptor-labeled proteins (each 1 μM) were incubated separately in PBS at 37 °C before measurement. The labeled αB oligomers were mixed in an equimolar ratio and incubated at 30 °C overnight to yield a saturated energy transfer by subunit exchange. On addition of a 25-fold molar excess of either unlabeled αB-WT or αB-3E to this FRET hetero-oligomers, fluorescence spectra were recorded at 37 °C using a Fluoromax 3 (Jobin Yvon). Data analysis was carried out according to Bova et al. (23).

Limited Proteolysis with α-Chymotrypsin. αB (10 μM) was incubated with α-chymotrypsin (Sigma) at a ratio of 1:25 (wt:wt) in 100 mM Tris, 100 mM NaCl, and 10 mM $CaCl_2$, pH 7.8, at 25 °C for 30 min. Proteolysis reactions were terminated with 2 mM phenylmethylsulfonyl fluoride (PMSF; Sigma) after various time points (0–45 min) and analyzed by SDS/PAGE on 15% acrylamide gels followed by Coomassie blue staining. The cleavage products and proteolysis sites were identified by LC-MS (*SI Materials and Methods*).

Aggregation Assays. All aggregation assays were carried out in a Varian Cary 50 UV/Vis spectrophotometer (Agilent) equipped with a temperature-adjustable cuvette holder. Aggregation of the substrate proteins was initiated by heat. The aggregation reaction was monitored at 350 nm over time as increasing signal caused by turbidity. The solubility of the clients after heat shock in the absence or presence of αB was assessed by SDS/PAGE and

Coomassie staining. Soluble and insoluble fractions were separated by centrifugation (10 min, 10,000 × *g*, 4 °C). The insoluble fraction was washed after the first centrifugation step by resuspending the pellet in PBS, followed by a second centrifugation step.

Thermal Aggregation of HeLa Lysates. HeLa cell lysate (*SI Materials and Methods*) was heat-stressed at 45 °C for 40 min in the presence of various amounts of αB. The soluble and insoluble protein fractions were separated and washed as described above.

Refolding of MDH. MDH (2 μM; in 25 mM Hepes, 50 mM KCl, 5 mM $MgCl_2$, and 1 mM DTT, pH 7.4) was incubated in the presence or absence of αB-WT or αB-3E (10 μM) at 46 °C for 45 min. MDH samples were cooled on ice and diluted 1:1 by adding the respective refolding mix containing combinations of Hsc70 (2 μM), Hdj1 (0.5 μM), phosphoenol pyruvate (3 mM), pyruvate kinase (20 μg/mL), and ATP (2 mM) and then shifted to 30 °C, and samples were taken after different time points. Ten microliters of each sample was mixed with 190 μL assay buffer (0.5 mM oxaloacetate and 0.2 mM NADH). The MDH activity was measured at 340 nm for 15 min at 30 °C in a Varian Cary 50 UV/VIS spectrophotometer (Agilent).

p53 Reactivation Assay. p53 (3 μM) was incubated at 42 °C for 30 min in the absence or presence of 15 μM αB-WT or αB-3E in 25 mM Hepes, 150 mM KCl, and 5 mM $MgCl_2$, pH 7.4. As a positive control, p53 was kept at 4 °C. Reactivation of p53 was performed using 2 μM Hsc70 and 0.5 μM Hdj1 in the presence of an ATP regenerative system (3 mM phosphoenol pyruvate, 20 μg/mL pyruvate kinase, and 2 mM ATP) in 25 mM Hepes, 150 mM KCl, 5 mM $MgCl_2$, and 1 mM DTT, pH 7.4, for 270 min at 30 °C and 30 min at 25 °C. For determination of p53 DNA-binding activity, an EMSA was performed (*SI Materials and Methods*).

ACKNOWLEDGMENTS. We thank Marc Wehmer, Sonja Schmid, and Franziska Tippel for general experimental help, Oliver Lorenz for providing purified Hsc70, and Eva Kriehuber for HeLa cells. J.B. and S.W. are funded by the Deutsche Forschungsgemeinschaft (SFB1035). J.P. acknowledges a PhD scholarship from the Studienstiftung des deutschen Volkes.

1. Hartl FU, Bracher A, Hayer-Hartl M (2011) Molecular chaperones in protein folding and proteostasis. *Nature* 475(7356):324–332.
2. Richter K, Haslbeck M, Buchner J (2010) The heat shock response: Life on the verge of death. *Mol Cell* 40(2):253–266.
3. Tyedmers J, Mogk A, Bukau B (2010) Cellular strategies for controlling protein aggregation. *Nat Rev Mol Cell Biol* 11(11):777–788.
4. Horwitz J (1992) Alpha-crystallin can function as a molecular chaperone. *Proc Natl Acad Sci USA* 89(21):10449–10453.
5. Clark AR, Lubsen NH, Slingsby C (2012) sHSP in the eye lens: Crystallin mutations, cataract and proteostasis. *Int J Biochem Cell Biol* 44(10):1687–1697.
6. Iwaki T, Kume-Iwaki A, Liem RK, Goldman JE (1989) Alpha B-crystallin is expressed in non-lenticular tissues and accumulates in Alexander's disease brain. *Cell* 57(1):71–78.
7. Goldstein LE, et al. (2003) Cytosolic beta-amyloid deposition and supranuclear cataracts in lenses from people with Alzheimer's disease. *Lancet* 361(9365):1258–1265.
8. Ousman SS, et al. (2007) Protective and therapeutic role for alphaB-crystallin in autoimmune demyelination. *Nature* 448(7152):474–479.
9. Vicart P, et al. (1998) A missense mutation in the alphaB-crystallin chaperone gene causes a desmin-related myopathy. *Nat Genet* 20(1):92–95.
10. Launay N, Tarze A, Vicart P, Lilienbaum A (2010) Serine 59 phosphorylation of alphaB-crystallin down-regulates its anti-apoptotic function by binding and sequestering Bcl-2 in breast cancer cells. *J Biol Chem* 285(48):37324–37332.
11. Lin DI, et al. (2006) Phosphorylation-dependent ubiquitination of cyclin D1 by the SCF (FBX4-alphaB crystallin) complex. *Mol Cell* 24(3):355–366.
12. de Jong WW, Caspers GJ, Leunissen JA (1998) Genealogy of the alpha-crystallin—small heat-shock protein superfamily. *Int J Biol Macromol* 22(3-4):151–162.
13. Kriehuber T, et al. (2010) Independent evolution of the core domain and its flanking sequences in small heat shock proteins. *FASEB J* 24(10):3633–3642.
14. Jehle S, et al. (2010) Solid-state NMR and SAXS studies provide a structural basis for the activation of alphaB-crystallin oligomers. *Nat Struct Mol Biol* 17(9):1037–1042.
15. Bagnéris C, et al. (2009) Crystal structures of alpha-crystallin domain dimers of alphaB-crystallin and Hsp20. *J Mol Biol* 392(5):1242–1252.
16. Laganowsky A, et al. (2010) Crystal structures of truncated alphaA and alphaB crystallins reveal structural mechanisms of polydispersity important for eye lens function. *Protein Sci* 19(5):1031–1043.
17. Braun N, et al. (2011) Multiple molecular architectures of the eye lens chaperone αB-crystallin elucidated by a triple hybrid approach. *Proc Natl Acad Sci USA* 108(51):20491–20496.
18. Jehle S, et al. (2011) N-terminal domain of alphaB-crystallin provides a conformational switch for multimerization and structural heterogeneity. *Proc Natl Acad Sci USA* 108(16):6409–6414.
19. Delbecq SP, Klevit RE (2013) One size does not fit all: The oligomeric states of αB crystallin. *FEBS Lett* 587(8):1073–1080.
20. Aquilina JA, Benesch JL, Bateman OA, Slingsby C, Robinson CV (2003) Polydispersity of a mammalian chaperone: Mass spectrometry reveals the population of oligomers in alphaB-crystallin. *Proc Natl Acad Sci USA* 100(19):10611–10616.
21. Horwitz J (2009) Alpha crystallin: The quest for a homogeneous quaternary structure. *Exp Eye Res* 88(2):190–194.
22. Peschek J, et al. (2009) The eye lens chaperone alpha-crystallin forms defined globular assemblies. *Proc Natl Acad Sci USA* 106(32):13272–13277.
23. Bova MP, Ding LL, Horwitz J, Fung BK (1997) Subunit exchange of alphaA-crystallin. *J Biol Chem* 272(47):29511–29517.
24. Baldwin AJ, et al. (2011) Quaternary dynamics of αB-crystallin as a direct consequence of localised tertiary fluctuations in the C-terminus. *J Mol Biol* 413(2):310–320.
25. Cheng G, Basha E, Wysocki VH, Vierling E (2008) Insights into small heat shock protein and substrate structure during chaperone action derived from hydrogen/deuterium exchange and mass spectrometry. *J Biol Chem* 283(39):26634–26642.
26. Jakob U, Gaestel M, Engel K, Buchner J (1993) Small heat shock proteins are molecular chaperones. *J Biol Chem* 268(3):1517–1520.
27. Lee GJ, Roseman AM, Saibil HR, Vierling E (1997) A small heat shock protein stably binds heat-denatured model substrates and can maintain a substrate in a folding-competent state. *EMBO J* 16(3):659–671.
28. Ehrnsperger M, Gräber S, Gaestel M, Buchner J (1997) Binding of non-native protein to Hsp25 during heat shock creates a reservoir of folding intermediates for reactivation. *EMBO J* 16(2):221–229.
29. Jaya N, Garcia V, Vierling E (2009) Substrate binding site flexibility of the small heat shock protein molecular chaperones. *Proc Natl Acad Sci USA* 106(37):15604–15609.
30. Basha E, Friedrich KL, Vierling E (2006) The N-terminal arm of small heat shock proteins is important for both chaperone activity and substrate specificity. *J Biol Chem* 281(52):39943–39952.
31. McHaourab HS, Godar JA, Stewart PL (2009) Structure and mechanism of protein stability sensors: Chaperone activity of small heat shock proteins. *Biochemistry* 48(18):3828–3837.
32. Ahrman E, Lambert W, Aquilina JA, Robinson CV, Emanuelsson CS (2007) Chemical cross-linking of the chloroplast localized small heat-shock protein, Hsp21, and the model substrate citrate synthase. *Protein Sci* 16(7):1464–1478.
33. McDonald ET, Bortolus M, Koteiche HA, Mchaourab HS (2012) Sequence, structure, and dynamic determinants of Hsp27 (HspB1) equilibrium dissociation are encoded by the N-terminal domain. *Biochemistry* 51(6):1257–1268.
34. Franzmann TM, Menhorn P, Walter S, Buchner J (2008) Activation of the chaperone Hsp26 is controlled by the rearrangement of its thermosensor domain. *Mol Cell* 29(2):207–216.
35. Bepperling A, et al. (2012) Alternative bacterial two-component small heat shock protein systems. *Proc Natl Acad Sci USA* 109(50):20407–20412.
36. Kampinga HH, Garrido C (2012) HSPBs: Small proteins with big implications in human disease. *Int J Biochem Cell Biol* 44(10):1706–1710.
37. Ito H, Okamoto K, Nakayama H, Isobe T, Kato K (1997) Phosphorylation of alphaB-crystallin in response to various types of stress. *J Biol Chem* 272(47):29934–29941.
38. Kato K, et al. (1998) Phosphorylation of alphaB-crystallin in mitotic cells and identification of enzymatic activities responsible for phosphorylation. *J Biol Chem* 273(43):28346–28354.
39. Ito H, et al. (2001) Phosphorylation-induced change of the oligomerization state of alpha B-crystallin. *J Biol Chem* 276(7):5346–5352.
40. Ahmad MF, Raman B, Ramakrishna T, Rao ChM (2008) Effect of phosphorylation on alpha B-crystallin: Differences in stability, subunit exchange and chaperone activity of homo and mixed oligomers of alpha B-crystallin and its phosphorylation-mimicking mutant. *J Mol Biol* 375(4):1040–1051.
41. Ecroyd H, et al. (2007) Mimicking phosphorylation of alphaB-crystallin affects its chaperone activity. *Biochem J* 401(1):129–141.
42. Aquilina JA, et al. (2004) Phosphorylation of alphaB-crystallin alters chaperone function through loss of dimeric substructure. *J Biol Chem* 279(27):28675–28680.
43. Delbecq SP, Jehle S, Klevit R (2012) Binding determinants of the small heat shock protein, αB-crystallin: Recognition of the 'IxI' motif. *EMBO J* 31(24):4587–4594.
44. MacCoss MJ, et al. (2002) Shotgun identification of protein modifications from protein complexes and lens tissue. *Proc Natl Acad Sci USA* 99(12):7900–7905.
45. Stryer L (1965) The interaction of a naphthalene dye with apomyoglobin and apohemoglobin. A fluorescent probe of non-polar binding sites. *J Mol Biol* 13(2):482–495.
46. Schönbrunn E, Eschenburg S, Luger K, Kabsch W, Amrhein N (2000) Structural basis for the interaction of the fluorescence probe 8-anilino-1-naphthalene sulfonate (ANS) with the antibiotic target MurA. *Proc Natl Acad Sci USA* 97(12):6345–6349.
47. Simonetti A, et al. (2008) Structure of the 30S translation initiation complex. *Nature* 455(7211):416–420.
48. Koteiche HA, McHaourab HS (2003) Mechanism of chaperone function in small heat-shock proteins. Phosphorylation-induced activation of two-mode binding in alphaB-crystallin. *J Biol Chem* 278(12):10361–10367.
49. Bullock AN, Fersht AR (2001) Rescuing the function of mutant p53. *Nat Rev Cancer* 1(1):68–76.
50. Hagn F, et al. (2011) Structural analysis of the interaction between Hsp90 and the tumor suppressor protein p53. *Nat Struct Mol Biol* 18(10):1086–1093.
51. Watanabe G, et al. (2009) alphaB-crystallin: A novel p53-target gene required for p53-dependent apoptosis. *Cancer Sci* 100(12):2368–2375.
52. Stokoe D, Engel K, Campbell DG, Cohen P, Gaestel M (1992) Identification of MAPKAP kinase 2 as a major enzyme responsible for the phosphorylation of the small mammalian heat shock proteins. *FEBS Lett* 313(3):307–313.

53. Mogk A, et al. (2003) Refolding of substrates bound to small Hsps relies on a disaggregation reaction mediated most efficiently by ClpB/DnaK. *J Biol Chem* 278(33): 31033–31042.
54. Basha E, O'Neill H, Vierling E (2012) Small heat shock proteins and α-crystallins: Dynamic proteins with flexible functions. *Trends Biochem Sci* 37(3):106–117.
55. Eyles SJ, Gierasch LM (2010) Nature's molecular sponges: Small heat shock proteins grow into their chaperone roles. *Proc Natl Acad Sci USA* 107(7):2727–2728.
56. Haslbeck M, Franzmann T, Weinfurtner D, Buchner J (2005) Some like it hot: The structure and function of small heat-shock proteins. *Nat Struct Mol Biol* 12(10):842–846.
57. Hayes D, Napoli V, Mazurkie A, Stafford WF, Graceffa P (2009) Phosphorylation dependence of hsp27 multimeric size and molecular chaperone function. *J Biol Chem* 284(28):18801–18807.
58. Chen L, et al. (2011) Structural instability tuning as a regulatory mechanism in protein-protein interactions. *Mol Cell* 44(5):734–744.
59. Reichmann D, et al. (2012) Order out of disorder: Working cycle of an intrinsically unfolded chaperone. *Cell* 148(5):947–957.
60. Tapley TL, et al. (2009) Structural plasticity of an acid-activated chaperone allows promiscuous substrate binding. *Proc Natl Acad Sci USA* 106(14):5557–5562.
61. Uversky VN (2011) Intrinsically disordered proteins from A to Z. *Int J Biochem Cell Biol* 43(8):1090–1103.
62. Bardwell JC, Jakob U (2012) Conditional disorder in chaperone action. *Trends Biochem Sci* 37(12):517–525.
63. Tompa P, Csermely P (2004) The role of structural disorder in the function of RNA and protein chaperones. *FASEB J* 18(11):1169–1175.
64. Beltrao P, et al. (2012) Systematic functional prioritization of protein posttranslational modifications. *Cell* 150(2):413–425.
65. Bryantsev AL, et al. (2007) Regulation of stress-induced intracellular sorting and chaperone function of Hsp27 (HspB1) in mammalian cells. *Biochem J* 407(3):407–417.
66. King FW, Wawrzynow A, Höhfeld J, Zylicz M (2001) Co-chaperones Bag-1, Hop and Hsp40 regulate Hsc70 and Hsp90 interactions with wild-type or mutant p53. *EMBO J* 20(22):6297–6305.
67. Müller L, Schaupp A, Walerych D, Wegele H, Buchner J (2004) Hsp90 regulates the activity of wild type p53 under physiological and elevated temperatures. *J Biol Chem* 279(47):48846–48854.
68. Pandya MJ, et al. (2009) Interaction of human heat shock protein 70 with tumor-associated peptides. *Biol Chem* 390(4):305–312.
69. Retzlaff M, et al. (2013) The regulatory domain stabilizes the p53 tetramer by intersubunit contacts with the DNA binding domain. *J Mol Biol* 425(1):144–155.
70. Eisenberg D, Schwarz E, Komaromy M, Wall R (1984) Analysis of membrane and surface protein sequences with the hydrophobic moment plot. *J Mol Biol* 179(1): 125–142.
71. Wilkins MR, et al. (1999) Protein identification and analysis tools in the ExPASy server. *Methods Mol Biol* 112:531–552.